

Vacuum Rabi Splitting and Quantum Fisher Information of a Non-Hermitian Qubit in a Single-Mode Cavity

Yi-Cheng Wang and Jiong Li

*Zhejiang Key Laboratory of Micro-Nano Quantum Chips and Quantum Control,
School of Physics, Zhejiang University, Hangzhou 310027, China*

Li-Wei Duan

Department of Physics, Zhejiang Normal University, Jinhua 321004, China

Qing-Hu Chen*

*Zhejiang Key Laboratory of Micro-Nano Quantum Chips and Quantum Control,
School of Physics, Zhejiang University, Hangzhou 310027, China and
Collaborative Innovation Center of Advanced Microstructures, Nanjing University, Nanjing 210093, China
(Dated: December 24, 2024)*

A natural extension of the non-Hermitian qubit is to place it in a single-mode cavity. This setup corresponds to the quantum Rabi model (QRM) with a purely imaginary bias on the qubit, exhibiting the parity-time (\mathcal{PT}) symmetry. In this work, we first solve the \mathcal{PT} symmetric QRM using the Bogoliubov operator approach. We derive the transcendental function responsible for the exact solution, which can also be used to precisely identify exceptional points. The adiabatic approximation previously used can be easily formulated within this approach by considering transitions between the same manifolds in the space of Bogoliubov operators. By further considering transitions between the nearest-neighboring manifolds, we can analytically obtain more accurate eigen-solutions. Moreover, these simple corrections can capture the main features of the dynamics, where the adiabatic approximation fails. Furthermore, the rich characteristics of the vacuum Rabi splitting in the emission spectrum is predicted. The width of the peaks increases with the coupling strength and the imaginary biases, reflecting the nature of open quantum systems. Additionally, we identify a quantum criticality-enhanced effect by calculating the quantum Fisher information. Near the exceptional points, the quantum Fisher information in the \mathcal{PT} symmetric QRM is significantly higher than that of the non-Hermitian qubit component. This may open a new avenue for enhancing quantum sensitivity in non-Hermitian systems by incorporating coupling with an additional degree of freedom, enabling more precise parameter estimation.

I. INTRODUCTION

In recent years, concepts from non-Hermitian physics and parity-time (\mathcal{P} \mathcal{T})-symmetry have attracted considerable interest. Bender et al. demonstrated that a non-Hermitian Hamiltonian invariant under combined space reflection and time reversal can exhibit a real spectrum [1]. This counterintuitive result challenges the traditional view that real eigenvalues are associated exclusively with Hermitian observables, marking a significant milestone in non-Hermitian physics [2–6].

Unlike the strict mathematical requirement in traditional quantum physics that a Hamiltonian operator should be Hermitian, the \mathcal{PT} invariance condition is a weaker, more physically intuitive constraint, providing a rich field for both theoretical and experimental exploration. As system parameters vary, the \mathcal{PT} -symmetric system can transition between the \mathcal{PT} -unbroken and \mathcal{PT} -broken phases. In the \mathcal{PT} -unbroken phase, the system has real eigenvalues, while in the \mathcal{PT} -broken phase, it has a pair of conjugate eigenvalues. Phase transitions are characterized by numerous accumu-

lation points of exceptional points (EPs). At these EPs, both eigenvectors and eigenvalues coalesce. Additionally, dimensionality reduction occurs in the eigenspace of the EPs [7, 8].

Non-Hermitian \mathcal{PT} -symmetry has recently received considerable attention in the study of \mathcal{PT} -symmetric systems involving the interaction of qubits with classical light fields. [9–12]. This research belongs to the context of the non-Hermitian semi-classical Rabi model. \mathcal{PT} -symmetry in pure quantum systems, particularly in the context of light-matter interaction with an imaginary qubit-cavity coupling, has also been studied. Examples include the non-Hermitian Jaynes-Cummings model [13], the non-Hermitian double Jaynes-Cummings model [14], the dissipative quantum Rabi model (QRM) [15], and the non-Hermitian QRM [16].

The \mathcal{PT} -symmetric quantum Rabi model (PTQRM) with a purely imaginary bias [17] has rarely been explored. This model is, however, effectively a natural extension of the well-studied non-Hermitian two-level system (NH-TLS) coupled to a quantized light field. The PTQRM exhibits intriguing non-Hermitian properties, including an infinite number of EPs that vanish and reappear depending on the strength of the light-matter coupling. Furthermore, the PTQRM can be realized in realistic physical systems [17]. Potential physical

* qhchen@zju.edu.cn

implementations of the non-Hermitian Hamiltonian for the PTQRM include circuit quantum electrodynamics (cQED) [18], trapped-ion experiments, and the replacement of traditional qubits in QRM setups [18–22].

In this work, we extend the Bogoliubov operator approach (BOA) [23–25] to solve the PTQRM [17], and obtain the exact eigen-solutions and the EPs. Within this framework, we analytically propose a correction to the previous adiabatic approximation (AA), especially the eigenstates, leading to a deeper understanding of dynamics. We primarily investigate two prominent quantum effects of this model using our developed approaches: vacuum Rabi splitting (VRS), a key phenomenon in atomic physics [26], and Quantum Fisher information (QFI), which plays a crucial role in quantum metrology. Recent proposals suggest that quantum sensors based on non-Hermitian systems may exhibit enhanced sensitivity [27–35]. We calculate the QFI for both the ground and excited states of the system, with a particular focus on the QFI near the EPs [15, 29].

This paper is organized as follows: In Sec. II, we derive the transcendental function whose zeros provide the complete spectrum, using the Bogoliubov operator approach (BOA). The EPs are identified through their real number form in the \mathcal{PT} -unbroken phase. The previously often used AA is further corrected analytically. In Sec. III, we examine the atomic dynamics and the VRS in the emission spectrum using several approaches. The novel characteristics of the VRS are explored and discussed in terms of analytical eigenstates. In Sec. IV, we calculate the QFI in the PTQRM and its Hermitian counterpart, as well as for the NH-TLS, and perform the comparison of the QFI values near the EPs. Finally, a brief summary is provided in Sec. V. The appendix presents the determinant of the CAA and the selection rules for the eigenstates.

II. ANALYTICAL SOLUTION

The non-Hermitian qubit in a single-mode cavity can be described by the following Hamiltonian

$$H = -\frac{\Delta}{2}\sigma_x + \frac{i\epsilon}{2}\sigma_z + \omega a^\dagger a + g(a^\dagger + a)\sigma_z, \quad (1)$$

where the first two terms represent a non-Hermitian qubit with energy splitting Δ and an imaginary bias $i\epsilon$, $\sigma_{x,z}$ are the Pauli matrices, a^\dagger and a denote the creation and annihilation operators with cavity frequency ω , and g represents the qubit-cavity coupling strength. Its Hermitian counterpart is just the asymmetric QRM [23, 36–42]. For $\epsilon = 0$, the Hamiltonian (1) exhibits \mathbb{Z}_2 symmetry [43]. The conserved parity operator is defined as $\hat{P} = -\sigma_x \exp(i\pi a^\dagger a)$, with eigenvalues ± 1 . This symmetry allows the Hamiltonian (1) to be diagonalized into two blocks, each corresponding to a different parity subspace. Due to this \mathbb{Z}_2 symmetry, eigenvalues from different symmetry parity are allowed to cross.

When a pure imaginary bias $\epsilon \neq 0$ is introduced, the parity operator \hat{P}_1 is no longer conserved. Combined with the standard time-reversal operator T , which takes the complex conjugate, and noting that $T^\dagger \hat{x} T = \hat{x}$ and $T^\dagger \hat{p} T = -\hat{p}$, where \hat{x} is the displacement operator and \hat{p} is the momentum operator, it can be verified that $[H, \mathcal{PT}] = 0$. Therefore, the non-Hermitian Hamiltonian (1) is indeed \mathcal{PT} -symmetric, and is thus termed the PTQRM.

The PTQRM can be implemented in a practical system as proposed in Ref. [17]. After performing a rotation around the y -axis in the atomic sector, the Hamiltonian (1) transforms into their Eq. (1). Consider a passive \mathcal{PT} -symmetric qubit with the Hamiltonian $H_q^p = -\frac{\Delta}{2}\sigma_x + i\epsilon\sigma_+\sigma_-$, which differs from the standard \mathcal{PT} -symmetric qubit by a constant shift of $i\epsilon/2$, but retains all the essential features of standard \mathcal{PT} symmetry, including EPs. Incorporating a cavity into this passive qubit leads to the QRM under passive \mathcal{PT} -symmetry, known as the passive PTQRM. Using the Lindblad master-equation approach, Lu et al. demonstrate that the effective Hamiltonian governing the dynamics is synonymous with the passive PTQRM in the rotating frame, and is equivalent to the standard PTQRM Hamiltonian [17]. These authors have also proposed a potential circuit QED realization in which the transmon qubit circuit is embedded in a cavity.

In this section, we present the exact solution and several analytical approximations to the PTQRM.

A. Exact Solutions by the BOA

By two Bogoliubov transformations

$$A_\pm = a \pm g/\omega, \quad (2)$$

the Hamiltonian (1) can be transformed into the following matrix form with units $\hbar = \omega = 1$.

$$H = \begin{pmatrix} A_+^\dagger A_+ + i\frac{\epsilon}{2} - g^2 & -\Delta/2 \\ -\Delta/2 & A_-^\dagger A_- - i\frac{\epsilon}{2} - g^2 \end{pmatrix}, \quad (3)$$

the wavefunction can be expressed as a series expansions in terms of the A_+ operator

$$|A_+\rangle = \left(\begin{array}{c} \sum_{n=0}^{\infty} \sqrt{n!} e_n |n\rangle_{A_+} \\ \sum_{n=0}^{\infty} \sqrt{n!} f_n |n\rangle_{A_+} \end{array} \right), \quad (4)$$

where e_n and f_n are the expansion coefficients. It can also be expressed in terms of the A_- operator.

$$|A_-\rangle = \left(\begin{array}{c} \sum_{n=0}^{\infty} (-1)^n \sqrt{n!} c_n |n\rangle_{A_-} \\ \sum_{n=0}^{\infty} (-1)^n \sqrt{n!} d_n |n\rangle_{A_-} \end{array} \right), \quad (5)$$

with two coefficients, c_n and d_n . The states $|n\rangle_{A_+}$ and $|n\rangle_{A_-}$ are known as extended coherent states, possessing the following properties:

$$|n\rangle_{A_{\pm}} = \frac{(A_{\pm}^{\dagger})^n}{\sqrt{n!}}|0\rangle_{A_{\pm}} = \frac{(a^{\dagger} \pm g)^n}{\sqrt{n!}}|0\rangle_{A_{\pm}}, \quad (6)$$

$$|0\rangle_{A_{\pm}} = e^{-(1/2)g^2 \mp ga^{\dagger}}|0\rangle_a,$$

where the vacuum state $|0\rangle_{A_{\pm}}$ in Bogoliubov operators A_{\pm} is well defined as the eigenstate of the original photon annihilation operator a , and is known as a pure coherent state [44].

By the Schrödinger equation, we get the linear relation for two coefficients e_m and f_m of Eq. (4) with the same index m as

$$e_m = \frac{\Delta}{2(m - g^2 + \frac{i\epsilon}{2} - E)} f_m, \quad (7)$$

and the coefficient f_m can be defined recursively

$$(m+1)f_{m+1} = \frac{1}{2g} \left(m + 3g^2 - \frac{i\epsilon}{2} - E - \frac{\Delta^2}{4(m - g^2 + \frac{i\epsilon}{2} - E)} \right) f_m - f_{m-1},$$

with $f_0 = 1$. Similarly, the two coefficients c_m and d_m of Eq. (5) satisfy

$$d_m = \frac{\Delta}{2(m - g^2 - \frac{i\epsilon}{2} - E)} c_m, \quad (8)$$

and the recursive relation is given by

$$(m+1)c_{m+1} = \frac{1}{2g} \left(m + 3g^2 + \frac{i\epsilon}{2} - E - \frac{\Delta^2}{4(m - g^2 - \frac{i\epsilon}{2} - E)} \right) c_m - c_{m-1},$$

with $c_0 = 1$.

If both wavefunctions (4) and (5) are true eigenfunctions for a non-degenerate eigenstate with eigenvalue E , they should differ only by a constant ratio, i.e. $|A_+\rangle = z|A_-\rangle$. Projecting both sides onto the original vacuum state $|0\rangle$, using $\sqrt{n!}\langle 0|n\rangle_{A_+} = (-1)^n\sqrt{n!}\langle 0|n\rangle_{A_-} = e^{-g^2/2}g^n$ and eliminating z gives

$$\sum_{n=0}^{\infty} e_n g^n \sum_{n=0}^{\infty} d_n g^n = \sum_{n=0}^{\infty} f_n g^n \sum_{n=0}^{\infty} c_n g^n. \quad (9)$$

Using Eqs. (7) and (8), one can derive the complex G-function of the PTQRM,

$$G = \left(\frac{\Delta}{2} \right)^2 \left[\sum_{n=0}^{\infty} \frac{f_n}{n - g^2 + \frac{i\epsilon}{2} - E} g^n \right] \times \left[\sum_{n=0}^{\infty} \frac{c_n}{n - g^2 - \frac{i\epsilon}{2} - E} g^n \right] - \sum_{n=0}^{\infty} f_n g^n \sum_{n=0}^{\infty} c_n g^n. \quad (10)$$

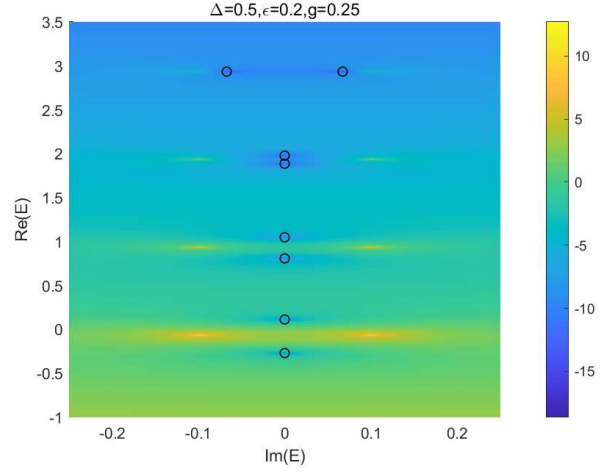


FIG. 1: $\ln|G|^2$, where G is calculated from the G-function (10), in the complex E plane. Open circles mark the zeros of both the real and imaginary parts of the G-function, which coincide exactly with the eigenvalues from the ED. The parameters are $\Delta = 0.5$, $\epsilon = 0.2$, and $g = 0.25$.

It includes both real and imaginary components. The zeros of this G-function provide both the real and imaginary components of the eigenvalues. As illustrated in Fig. 1, the eigenvalues obtained from the G-function (10) show excellent agreement with those from exact diagonalization (ED).

Notably, in the \mathcal{PT} -unbroken phase, it can be shown that

$$e_m = d_m^*,$$

$$f_m = c_m^*.$$

By following the same procedure, one can derive the real G-function in the form

$$G_{NH}^{(s)} = \left| \sum_{n=0}^{\infty} e_n g^n \right|^2 - \left| \sum_{n=0}^{\infty} f_n g^n \right|^2. \quad (11)$$

Although the coefficients e_n and f_n are complex, both terms in Eq. (11) represent squares of the modulus, making the G-function real. Its zeros can determine all real eigenvalues of this model within the \mathcal{PT} -unbroken region.

As shown in Fig. 2, all real eigenvalues (solid line) can be obtained by zeros of this real G-functions. EPs occur when both the G-function in Eq. (11) and its first-order derivative with respect to E are simultaneously zero, as illustrated in Fig. 2 (d). The zero of the first-order derivative identifies the EP where two real eigenvalues merge into one. Thus, using the real G-function Eq. (11), we can accurately pinpoint the position of the EPs and show that both eigenstates and eigenvalues coalesce at these points. It should be noted that, while we benefit from using the real G-function (11) to determine the EPs, it cannot be applied to \mathcal{PT} -broken region, marked by the dotted line in Fig. 2 (b) and the none solution in panel (e).

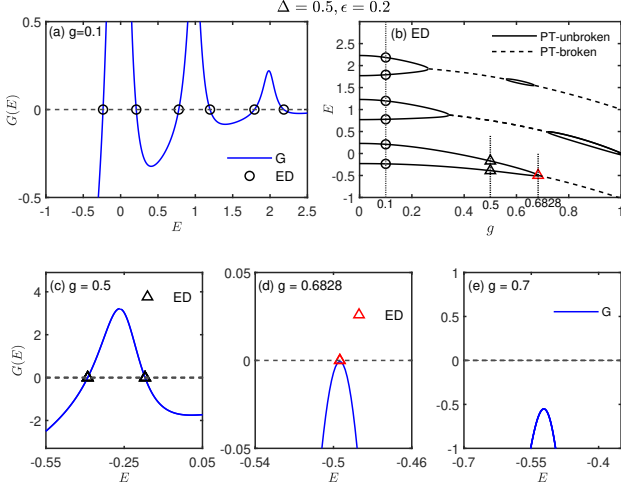


FIG. 2: (colored online) (a) G-curves from Eq. (11) (blue line) at $g = 0.1$ in the real eigenvalue regime, with circles representing ED results. (b) The real part of eigenvalues as a function of g from the ED, with the dashed lines marking the real part of eigenvalues in the \mathcal{PT} -broken region. Crossing values between the vertical dotted lines at $g = 0.1, 0.5$ and 0.6828 and real eigenvalues (solid line) in the \mathcal{PT} -unbroken region are confirmed in the G-functions in (a) and the lower panel. G-curves from Eq. (11) at $g = 0.5, 0.6828$ and 0.7 are shown in (c), (d), and (e) with blue lines, respectively. The parameters are $\Delta = 0.5$ and $\epsilon = 0.2$.

Finally, from Eqs. (7) and (8), it is clear that the denominator cannot vanish for any E due to the presence of the imaginary bias ϵ . As a result, the pole structure of the G-functions does not exist, in sharp contrast to its Hermitian counterpart [23, 36]. In other words, all eigenvalues can be given by the zeros of the general G-function (10), and all real eigenvalues in the \mathcal{PT} -unbroken phase can be obtained by zeros of the real G-function Eq.(11), even at the EPs, in the PTQRM. Note that the doubly degenerate solutions in its Hermitian counterpart cannot be given by the corresponding G-function [25, 38].

B. Adiabatic approximation method

A previous study of the PTQRM [17] primarily discussed the adiabatic approximation (AA). In this subsection, we present a simpler alternative to the AA method. Our goal is to establish a practical framework for the further correction and systematic improvement of the AA results.

Based on the matrix form of Eq. (3), the general wavefunction can also be expanded in terms of the two new operators A_+ and A_- simultaneously, as

$$|\Psi\rangle = \begin{pmatrix} \sum_{n=0} u_n |n\rangle_{A_+} \\ \sum_{n=0} (-1)^n v_n |n\rangle_{A_-} \end{pmatrix}. \quad (12)$$

This ansatz for the wavefunction is based on the extended

photonic coherent states in Eq. (6), which rely on various polaron-like transformations or shifted operators.

By the Schrödinger equation, we have

$$\left(m - g^2 + i\frac{\epsilon}{2}\right) u_m - \sum_{n=0} D_{mn} v_n = E u_m, \quad (13)$$

$$\left(m - g^2 - i\frac{\epsilon}{2}\right) v_m - \sum_{n=0} D_{mn} u_n = E v_m, \quad (14)$$

where

$$D_{mn} = \frac{\Delta}{2} (-1)^m {}_{A_-} \langle m | |n\rangle_{A_+},$$

$${}_{A_-} \langle m | |n\rangle_{A_+} = (2g)^{n-m} \exp(-2g^2) \sqrt{\frac{m!}{n!}} L_m^{n-m}(4g^2)$$

For $n \geq m$, $L_m^{n-m}(x)$ represents a Laguerre polynomial, with $D_{mn} = D_{nm}$. The term ${}_{A_-} \langle m | |n\rangle_{A_+}$ describes the overlap between the extended coherent states $|m\rangle_{A_+}$ and $|n\rangle_{A_-}$. We refer to both $|m\rangle_{A_+}$ and $|m\rangle_{A_-}$ as the m th manifold in the space of the Bogoliubov operators below.

Within the framework of Eqs. (13) and (14), analytical approximations can be systematically performed. First, as a zeroth-order approximation, we omit the off-diagonal terms and retain only the same m -th manifold,

$$|\Psi\rangle^{(AA)} = \begin{pmatrix} u_m |m\rangle_{A_+} \\ (-1)^m v_m |m\rangle_{A_-} \end{pmatrix}, \quad (15)$$

and have

$$\left(m - g^2 + i\frac{\epsilon}{2} - E\right) u_m - D_{m,m} v_m = 0, \quad (16)$$

$$-D_{m,m} u_m + \left(m - g^2 - i\frac{\epsilon}{2} - E\right) v_m = 0. \quad (17)$$

The nonzero coefficients u_m and v_m yield the following equation.

$$\left(m - g^2 + i\frac{\epsilon}{2} - E\right) \left(m - g^2 - i\frac{\epsilon}{2} - E\right) - (D_{m,m})^2 = 0.$$

The m -th pair of eigenvalues is then given by

$$E_{\pm} = m - g^2 \mp \frac{1}{2} \sqrt{4(D_{m,m})^2 - \epsilon^2}, \quad (18)$$

where $m = 0, 1, 2, \dots$, the corresponding m -th pair of eigenstates is

$$|m\rangle_{\pm} \propto \begin{pmatrix} (-1)^m D_{m,m} |m\rangle_{A_+} \\ (m - g^2 - i\frac{\epsilon}{2} - E_{\pm}) |m\rangle_{A_-} \end{pmatrix}. \quad (19)$$

Note that in Eq. (18), complex eigenvalues appear if $\epsilon > 2D_{m,m}$,

$$E_{\pm} = m - g^2 \mp \frac{i}{2} \sqrt{\epsilon^2 - 4(D_{m,m})^2}, \quad (20)$$

corresponding to the \mathcal{PT} -broken phase. Substituting E_+ into either Eq. (16) or Eq. (17) yields

$$\begin{aligned} (m - g^2 + i\frac{\epsilon}{2} - E_+) u_m - D_{m,m} v_m &= 0, \\ \frac{1}{2\eta} i \left(\sqrt{\epsilon^2 - 4(D_{m,m})^2} + \epsilon \right) u_m &= v_m. \end{aligned}$$

Set $c_m = 1$, we have

$$|\Psi\rangle^{(AA)} = N \begin{pmatrix} |m\rangle_{A+} \\ \frac{1}{2D_{m,m}} i \left(\sqrt{\epsilon^2 - 4(D_{m,m})^2} + \epsilon \right) |m\rangle_{A-} \end{pmatrix}, \quad (21)$$

where

$$N = \left[1 + \frac{1}{4D_{m,m}} \left(\sqrt{\epsilon^2 - 4(D_{m,m})^2} + \epsilon \right)^2 \right]^{-1/2}.$$

It can be confirmed that the wavefunction (21) lacks \mathcal{PT} -symmetry, even though the Hamiltonian still commutes with the \mathcal{PT} operator. This behavior contrasts with the case where the system is in the \mathcal{PT} -unbroken phase. As an approximate solution, it can be verified that $|m\rangle_{\pm}$ must coincide at the EPs where $\epsilon = 2\eta$, as given in Eq. (19).

Note that the zeroth-order approximation here is identical to the AA discussed by Lu et al. [17]. The transitions between different manifolds $|m\rangle_{A\pm}$ are omitted in this approximation of the wavefunction (15), which is commonly referred to as the adiabatic approximation.

The AA results for the eigenvalues, shown in Fig. 3 for $\epsilon = 0.1$ and $\epsilon = 0.5$, basically align with the ED results but still deviate in both the \mathcal{PT} -unbroken and \mathcal{PT} -broken region, except in the deep-strong coupling regime. There is still room for improving the AA. The key assumption of the AA is that only transitions between the two same manifolds are considered, while transitions between two different manifolds are neglected [45]. To obtain more accurate results, additional transitions must be included. Corrections to the AA method are discussed in the next subsection.

C. Corrections to the AA

The AA method can be incrementally improved by symmetrically including additional off-diagonal elements in the current formalism. The symmetric correction to the AA, referred to as CAA, is made by selecting three sets of coefficients: (u_{m-1}, v_{m-1}) , (u_m, v_m) and (u_{m+1}, v_{m+1}) , which represent symmetric transitions between the two nearest-neighboring manifolds and within the same manifold. $m \leftrightarrow m, m \pm 1$. In contrast, in the AA, the $(m \pm 1)$ -th manifold is not involved in the m -th pair of eigenvalues.

According to Eq. (12), the eigenstate corresponding to

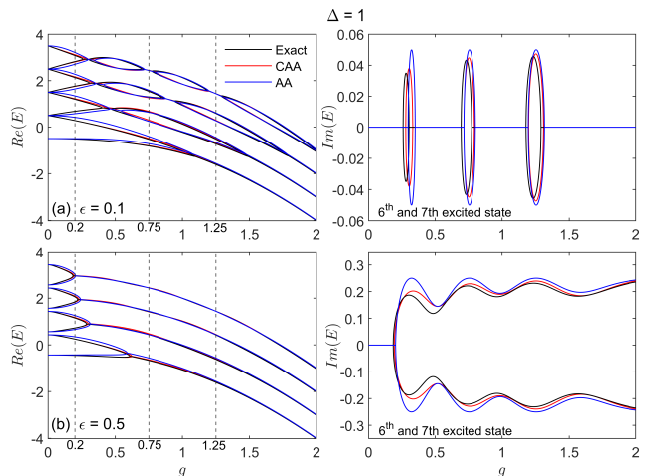


FIG. 3: (colored online) The real part (left panel) of the first four pairs and the imaginary part (right panel) of only the fourth pair of eigenvalues (for clarity) as a function of coupling strength g at resonance $\Delta = 1$ for $\epsilon = 0.1$ (upper panel) and $\epsilon = 0.5$ (lower panel). The black lines represent the ED results, the blue dots show the AA results, and the red dots indicate the CAA results. The eigenvalues and corresponding eigenstates along the dashed vertical line will be used to calculate the dynamics shown in Fig. 4, 5 and 6.

the m -th pair eigenvalues is selected as

$$|\Psi_{CAA}\rangle = \begin{pmatrix} u_{m-1} |m-1\rangle_{A+} + u_m |m\rangle_{A+} + u_{m+1} |m+1\rangle_{A+} \\ \mp v_{m-1} |m-1\rangle_{A-} \pm v_m |m\rangle_{A-} \mp v_{m+1} |m+1\rangle_{A-} \end{pmatrix}, \quad (22)$$

where the first \mp in the second line corresponds to odd and even m . The m -th pair of eigenvalues can be obtained by selecting the determinant in a 6×6 block form with $n = m, m \pm 1$ in Eqs. (13) and (14), as presented in the Appendix. This determinant leads to a polynomial equation of degree six. An explicit analytical solution cannot be obtained due to the Abel-Ruffini theorem, which asserts that no general solution in radicals exists for polynomial equations of degree five or higher with arbitrary coefficients [46]. There are six groups of roots, but only two are required. The CAA results should match the AA results from Eq. (18). This allows us to unambiguously identify the m -th pair of eigenvalues in the CAA from the full set of solutions. A simple selection rule is outlined in the Appendix.

Figure 3 shows that the CAA results for the eigenvalues align well with the exact ones in the entire coupling regimes. In particular, near the EPs, the CAA results show a marked improvement over the AA. However, the key improvement is not in the accuracy of the eigenvalues, but in the form of the eigenstates, which will be clearly illustrated in the dynamics.

Further corrections, such as the inclusion of five sets of coefficients, $(u_{m\pm i}, v_{m\pm i})$, $i = 0, 1, 2$, can also be implemented in a similar manner. In principle, these corrections can be applied systematically, step by step, ul-

timately converging to the exact solutions outlined in Subsection A. However, if a qualitative understanding of the physics is achieved within the CAA, additional corrections may be unnecessary in the analytical sense, as shown in the next section, where the CAA will also be used to calculate the qubit dynamics and study the VRS of the PTQRM.

III. DYNAMICS AND VACUUM RABI SPLITTING

One of the notable features in atom-cavity coupling system is the VRS, as described in [47–49]. The atom is typically pumped from its ground state to the excited state, and then decays to the ground state of the whole system. The resulting emission spectrum displays two peaks of equal height at resonance, characteristic of VRS in the Jaynes-Cummings model [26].

In this section, we calculate the time evolution of the qubit population difference, $\langle \sigma_z \rangle$, in the PTQRM using three methods: the CAA, AA, and exact solution, either ED or through the exact eigensolution obtained via the BOA. We use $|\psi_n^R\rangle$ and $|\psi_n^L\rangle$ to denote the right and left eigenstates, the eigenstates of H and H^\dagger , respectively. The normalization conditions are $\langle \psi_n^R | \psi_n^R \rangle = 1$ and $\langle \psi_m^L | \psi_n^R \rangle = \delta_{m,n}$, while the right and left eigenstates with different eigenvalues are non-orthogonal. That is $\langle \psi_m^{R(L)} | \psi_n^{R(L)} \rangle \neq 0$ for $m \neq n$, due to the non-Hermitian nature [50]. The time-dependent wave function of the PTQRM, starting from $|\Psi(0)\rangle$, can be expressed as

$$|\Psi(t)\rangle = e^{-iHt}|\Psi(0)\rangle = \sum_m e^{-itE_m} |\psi_m^R\rangle \langle \psi_m^L | \Psi(0)\rangle, \quad (23)$$

$\langle \sigma_z \rangle$ is thus given by

$$\langle \sigma_z(t) \rangle = \frac{\langle \psi(t) | \sigma_z | \psi(t) \rangle}{\|\psi(t)\|^2}, \quad (24)$$

where $\|\psi(t)\| = \sqrt{\langle \psi(t) | \psi(t) \rangle}$ is the norm of the wavefunction, which is necessary in non-Hermitian systems. In general non-Hermitian Hamiltonians describe the dynamics of physical systems that are not conservative. The quantity $\langle \sigma_z(t) \rangle$ is related to the qubit population in the literature through the expression $(1 + \langle \sigma_z(t) \rangle)/2$. This provides a more direct measure of the upper state the qubit.

To analyze the dynamic behavior in more detail, a Fourier spectral analysis of the atomic population's time evolution is performed. The Fourier transform, a key technique for frequency decomposition, is defined as follows:

$$\mathcal{F}(\nu) = \int_0^\infty \langle \sigma_z(t) \rangle e^{-i2\pi\nu t} dt,$$

where $\mathcal{F}(\nu)$ represents the emission spectrum, and $F(t)$ denotes the observed time evolution.

The initial state is chosen as the atomic upper level and the photon vacuum state in the PTQRM, similar to the conventional study of the VRS. The dynamical evolution at resonance ($\Delta = 1$) is calculated using the CAA for two imaginary biases, $\epsilon = 0.1$ and $\epsilon = 0.5$, and three typical coupling strengths: $g = 0.1, 0.75$, and 1.25 . These coupling strengths range from the ultrastrong to deep-strong coupling regimes. The results (red line) for the dynamics are respectively shown in the left panel of Figs.4, 5, and 6, while the emission spectrum of the atomic population evolution is shown in the right panel of these three figures. Results from the ED (black dashed line) and AA (blue line) are also presented for comparison.

The present initial state has dominant components in the low-energy excited states of the system. In the early stages of evolution, it involves only the ground state and the lower excited states, with progressively higher excited states participating as time progresses. Generally, EPs shift toward lower coupling strengths (g) as the excited state number increases, as seen in the left panel of Fig. 3. As indicated by the vertical dashed line, the spectrum at $g = 0.2$ is partially in the \mathcal{PT} -unbroken phase for lower excited states, while the spectra at $g = 0.75$ and $g = 1.25$ are primarily in the \mathcal{PT} -broken phase for most lower excited states. We now proceed with the three typical coupling regimes.

Ultrastrong coupling regime ($g = 0.2$):- As shown in Fig. 4, the CAA results perfectly agree with the exact ones in both atomic dynamics and the emission spectrum. Oscillations with two main frequency are observed in the PTQRM, similar to the VRS in its Hermitian counterpart. This demonstrates that \mathcal{PT} -symmetry is preserved in the local phase during the early stages of the time evolution. In contrast, a oscillation with a single frequency is exhibited in the AA. Note that subharmonic peaks in the high frequency region of the emission spectrum result from the imperfect sinusoidal oscillations and do not indicate oscillations at new frequencies.

Interestingly, the positions of the two peaks in the CAA coincide with the crossing points of the vertical dashed line and the CAA eigenvalues in the left panel of Fig. 3, corresponding to the energies for the first and second excited states relative to the ground state energy, $E_1^{CAA} - E_{GS}^{CAA}$ and $E_2^{CAA} - E_{GS}^{CAA}$, respectively. In contrast, the position of the single peak in the AA reflects the difference between the first excited state energy (E_+) and the ground state energy (E_-), as given in Eq.(18), and is also shown in the left panel of Fig. 3. This occurs because, in the CAA, the nearest-neighboring manifold is considered, allowing transitions from both the first and second excited states to the ground state. In contrast, only the transition between the same manifold is taken into account in the AA, so the second excited state is excluded.

Near deep-strong coupling regime ($g = 0.75$):- As

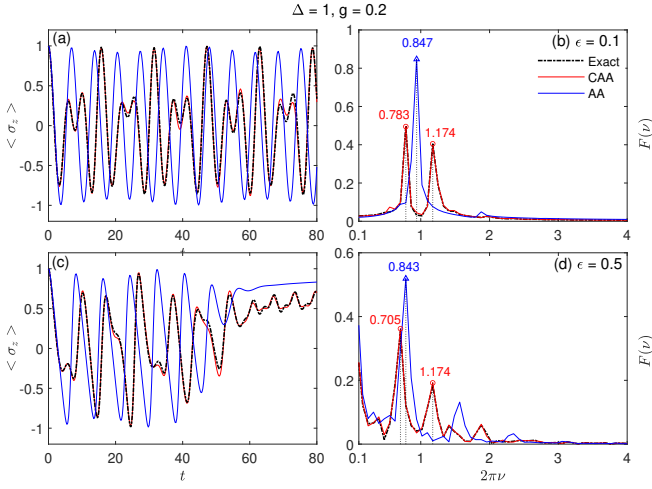


FIG. 4: (colored online) Time evolution of $\langle \sigma_z \rangle$ (left panel) and the corresponding emission spectrum (right panel) at resonance ($\Delta = 1$) for the ultrastrong coupling ($g = 0.2$) with $\epsilon = 0.1$ (upper panel) and $\epsilon = 0.5$ (lower panel). The peak positions are also shown in the left panel.

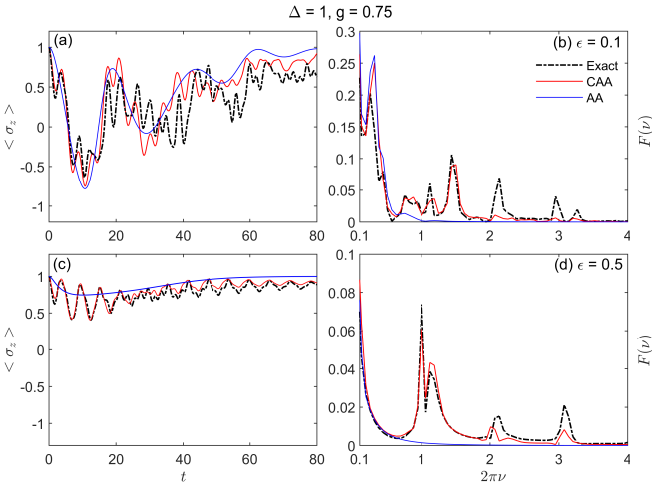


FIG. 5: (colored online) Time evolution of $\langle \sigma_z \rangle$ (left panel) and the corresponding emission spectrum (right panel) at resonance ($\Delta = 1$) for near deep-strong coupling ($g = 0.75$) with $\epsilon = 0.1$ (upper panel) and $\epsilon = 0.5$ (lower panel).

shown in the upper panel of Fig. 5 for both biases, the population from both the CAA and exact solutions oscillates with more than two frequencies, indicating multiple VRS. This is similar to the multiple Rabi oscillations observed in the ultrastrong coupling regime of its Hermitian counterpart without biases [51] and in systems with ultrastrong molecular vibrational coupling [52]. However, the frequency spectrum in the AA shows only one peak for $\epsilon = 0.1$, and the $\langle \sigma_z(t) \rangle$ curve tracks only the envelope of the multiple oscillations observed in the exact solutions, erasing the details of the fast oscillations. No peak at finite frequency is observed in the AA for large

bias $\epsilon = 0.5$.

Multiple peaks in the frequency spectrum arise in the CAA because higher m pairs of eigenstates are increasingly involved as the coupling strength increases, covering more manifolds than the $m = 0$ pair used in the ultrastrong coupling regime ($g = 0.2$). For example, the $m = 1$ pair of eigenstates spans the $m = 0, 1, 2$ manifolds, while the $m = 0$ pair only spans the $m = 0, 1$ manifolds.

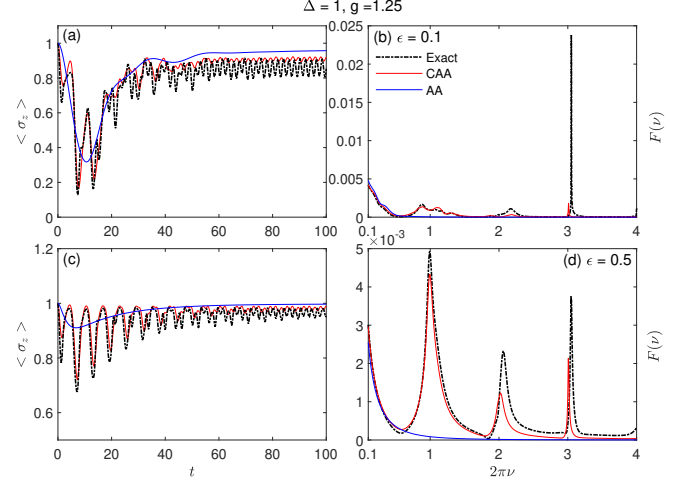


FIG. 6: (colored online) Time evolution of $\langle \sigma_z \rangle$ (left panel) and the corresponding emission spectrum (right panel) at resonance ($\Delta = 1$) for the deep-strong coupling ($g = 1.25$) with $\epsilon = 0.1$ (upper panel) and $\epsilon = 0.5$ (lower panel).

Deep-strong coupling regime $g = 1.25$: In this coupling regime, the atomic population difference never becomes negative, indicating that the atom predominantly stays in the upper level. The atomic population oscillates also with multiple frequencies. The CAA matches the exact solution, while the AA only captures the general envelope of the true dynamics, eliminating all the fast oscillations.

In the three typical coupling regimes discussed above, it is evident that the AA does not accurately capture the true behavior of atomic population evolution in this non-Hermitian model. The CAA results match the ED results in all cases. Although the eigenvalue difference between the AA and CAA is relatively small, the essential differences in dynamics can still depend on the number of manifolds considered. In other words, transitions within the same manifold are insufficient to describe the dynamics; transitions between different manifolds must also be considered in the analysis. Since the CAA provides an accurate and precise description of the dynamic behavior of the PTQRM in all cases, the additional consideration of transitions between nearest-neighboring manifolds is already sufficient to capture the key physics of the model.

In this non-Hermitian \mathcal{PT} -symmetric system, the atom tends to return to its original state, accompanied by an infinite number of photons [17]. This feature is clearly visible in Figs. 4 (c), 5, and 6 during the final time window. For the small bias and ultrastrong coupling regime,

we calculated the long-time evolution, continuing from the data in Figs. 4 (a), and observed similar behavior after a prolonged oscillation (not shown here). This represents the final outcome, likely due to the balance of gain and loss in the non-Hermitian system with \mathcal{PT} symmetry.

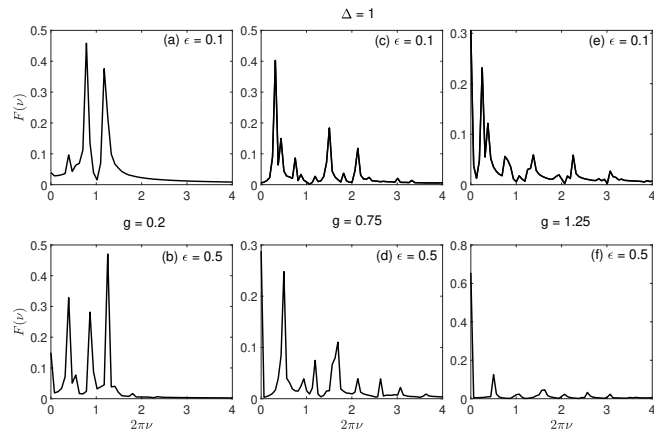


FIG. 7: The frequency spectrum of the Hermitian QRM at resonance ($\Delta = 1$) for ultrastrong coupling ($g = 0.2$), the near deep-strong coupling ($g = 0.75$), and the deep-strong coupling ($g = 1.25$), with $\epsilon = 0.1$ (upper panel) and $\epsilon = 0.5$ (lower panel).

As the coupling strength increases, the VRS splits into multiple Rabi frequencies. The width of the VRS peaks increases with both the bias and the coupling strength, due to the \mathcal{PT} -broken phases involved. As shown in Fig. 7 for its Hermitian counterpart with the same real biases, the VRS exhibits sharp peaks. Multiple VRS also emerges with ϵ , but the width remains unchanged. The peak width is typically determined by the decay rate. The imaginary bias, $i\epsilon$, effectively plays the role of a decay rate. The pronounced width of the VRS peaks resembles that of the VRS in two-level atoms of an atom-cavity system dissipating in a bosonic environment [53]. This suggests that non-Hermiticity can be viewed as an effective description of an open system, assuming quantum jumps are disregarded [54].

IV. QUANTUM FISHER INFORMATION AND ENHANCED QUANTUM SENSING

The QFI provides the optimal accuracy limit for parameter estimation and has significant applications in quantum precision measurement. [27, 29, 30, 34, 55]. In physical systems with critical properties, small changes in parameters near a critical point can cause significant responses in the quantum state, enabling the exploitation of this critical enhancement effect to improve parameter estimation accuracy. Increasing the QFI to improve the estimation accuracy of unknown parameters is a key issue in quantum metrology. Recent theoretical and ex-

perimental studies have shown that near EPs unique to non-Hermitian systems, the system exhibits a strong response to perturbations in parameters. Therefore, EPs can be used to achieve high-precision sensing [32, 33].

In quantum parameter estimation theory, the QFI describes the minimum error in extracting an unknown parameter from a given quantum state. The optimal measurement accuracy is governed by the quantum Cramér-Rao bound [29, 55, 56]. It can be proven that the expressions for both the traditional QFI and the parameter estimates of the quantum Cramér-Rao bound still hold for non-Hermitian Hamiltonians under stationary-states [29, 57]. Thus, for the PTQRM, the QFI for the pure states is defined as

$$\mathcal{F}_\lambda(|\psi\rangle) = 4 \left(\langle \psi'(\lambda) | \psi'(\lambda) \rangle - |\langle \psi'(\lambda) | \psi(\lambda) \rangle|^2 \right), \quad (25)$$

where λ represents the experimental parameter to be estimated. In the present study, we select $\lambda = g$, $|\psi(g)\rangle$ is one eigenstate and $|\psi'(g)\rangle$ is its first-order derivative with respect to the coupling strength g . As mentioned previously, for a non-Hermitian Hamiltonian ($H^\dagger \neq H$), the eigenstates are typically non-orthogonal. Under the stationary state condition, the normalization condition of the eigenstates holds, and it can be proven that the QFI still satisfies Eq. (25). We have verified that $|\psi(g)\rangle$ can be selected either the right or the left eigenstates of the PTQRM, the QFI remains unchanged.

Figure 8 (a) illustrates the QFIs in the ground state for both the Hermitian QRM and PTQRM, calculated using the wavefunction derived from the G-function technique or the ED. The results are shown for $\Delta = 0.5$ and various bias parameters ($\epsilon = 0, 0.2, 0.4$). The QFI in the PTQRM are noticeably higher than those in the Hermitian QRMs, both in the symmetric case ($\epsilon = 0$) and the asymmetric case ($\epsilon \neq 0$). Near the EPs $g = 0.6828$ for $\epsilon = 0.2$ and $g = 0.3358$ for $\epsilon = 0.4$, the QFI in the PTQRM exhibits a sharp peak. This indicates that the PT-symmetric non-Hermitian system is highly sensitive to perturbations in the estimated parameter near the EP. This effect is known as \mathcal{PT} -enhanced quantum sensing [32, 34, 35]. In the Hermitian QRM, the QFI shows a shallow maximum. The Hermitian QRM shows only a crossover, without a phase transition exhibiting a singularity. In contrast, the EPs of the PTQRM mark the transition from the \mathcal{PT} -unbroken phase to the \mathcal{PT} -broken phase. Figure 8 (b) shows that the QFI in the fourth excited state near the first EP is significantly higher than that in the ground state for the same model parameters. This implies that using the higher excited state can improve the estimation accuracy of unknown parameters.

Since the PTQRM can be viewed as a NH-TLS coupled to a quantized cavity. A natural question arises: can quantum sensing for the NH-TLS be enhanced through coupling with the cavity. To address this issue, we calculate the QFI for both the NH-TLS and PTQRM, where the former is a component of the latter. To provide a

clear comparison, we derive the analytical QFI for the NH-TLS and PTQRM in the AA below,

$$F_{\epsilon}^{NH-TLS} = \begin{cases} \frac{1}{4(\Delta^2 - \epsilon^2)}, & \epsilon \leq \Delta \\ \frac{\Delta^2}{4\epsilon^2(\epsilon^2 - \Delta^2)}, & \epsilon > \Delta \end{cases} \quad (26)$$

and

$$F_{\epsilon}^{PTQRM} = \begin{cases} \frac{1}{4(\Delta^2 e^{-4g^2} - \epsilon^2)}, & \epsilon \leq \Delta e^{-2g^2} \\ \frac{\Delta^2 - g^2}{4\epsilon^2(\epsilon^2 - \Delta^2 e^{-4g^2})}, & \epsilon > \Delta e^{-2g^2} \end{cases} \quad (27)$$

where EPs are given by $\epsilon_{EP} = \Delta$ for the NH-TLS and Δe^{-2g^2} for the PTQRM.

In the \mathcal{PT} -unbroken regime ($\epsilon \leq \epsilon_{EP}$), let ϵ deviate slightly from the EP by a small amount δ ; thus, the QFI becomes

$$F_{\epsilon=\Delta e^{-2g^2} - \delta}^{PTQRM} = (8\Delta\delta)^{-1} e^{2g^2}$$

for the PTQRM in the AA, and

$$F_{\epsilon=\Delta - \delta}^{NH-TLS} = (8\Delta\delta)^{-1},$$

for the NH-TLS. Here, higher-order terms in small δ is neglected. The QFI is finite as long as $\delta \neq 0$. It is evident that the QFI in the PTQRM is higher than that in the NH-TLS, with an enhanced factor of e^{2g^2} . At weak coupling, the enhanced factor can be neglected; however, it becomes more pronounced as the coupling strength increases. Clearly, these findings also apply to the \mathcal{PT} -broken regime.

The numerically exact QFI (solid colored line) and the analytical QFI in the AA (dashed line) for the PTQRM are shown in Fig. 8 (c), along with the QFI for the NH-TLS (black solid line) for comparison. At weak coupling ($g = 0.1$), the QFI remains nearly unaffected by the cavity coupling but increases as the coupling strength grows. In the deep-strong coupling regime ($g = 1.0$), the QFI is significantly higher than that in the NH-TLS. This can be more clear if we normalize the bias value to the peak position (also at EP), as shown in Fig. 8 (d). Strong qubit-cavity coupling offers a novel method to enhance quantum sensing in the extensively studied NH-TLS. Note that the QFI calculated by the AA is quite accurate because only the same eigenstates are used.

Finally, the QFI can serve as a signature for the EPs. This indicates that the quantum critically enhanced effect can locate the EPs of the PTQRM, offering an alternative to the G-function technique discussed in Sec. II(a). As illustrated in Fig. 8 (b), the QFI at $\epsilon = 0.2$ for both the ground state and the excited state display sharp peaks exactly at the corresponding EPs, which align perfectly with the EPs in Fig. 2 (b).

V. CONCLUSION

We use the Bogoliubov operator approach to derive the G-function for the PTQRM, whose zeros exactly determine the eigenvalues in both the \mathcal{PT} -symmetric and

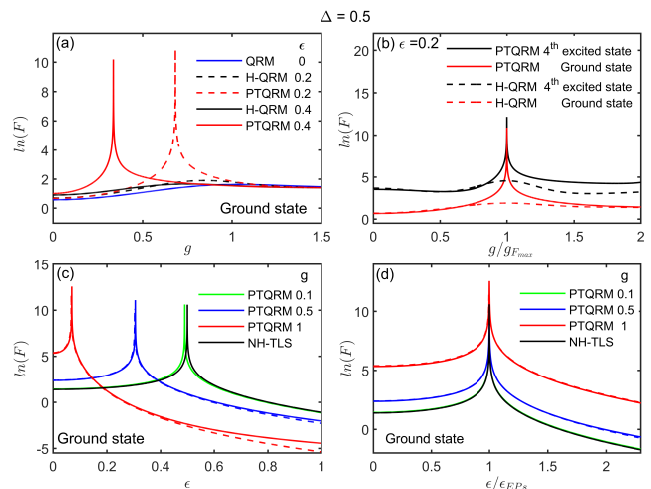


FIG. 8: (colored online) (Upper panel) The QFI as a function of coupling strength g : (a) in the ground state, with $\epsilon = 0.2$ (dashed line) and $\epsilon = 0.4$ (solid line). The black line corresponds to the Hermitian QRM, the red line to the PTQRM, and the blue line to the symmetric QRM; (b) In the 4th excited state (black lines) and the ground state (red lines) for the Hermitian QRM (solid line) and the PTQRM (dashed line) at $\epsilon = 0.2$ and $\Delta = 0.5$. The QFI is scaled by $\epsilon/\epsilon_{F_{max}}$. (Lower panel) The QFI as a function of bias ϵ : (c) in the ground state for $g = 0.1$ (green line), 0.5 (blue line), and 1 (red line) in the PTQRM, and for NH-TLS (black line). Dashed lines represent the corresponding analytical results for the PTQRM (Eq. (27)) and NH-TLS (Eq. (26)); (d) The QFI from (c) scaled by ϵ/ϵ_{EP} , where ϵ_{EP} is the corresponding exact value for the EP.

\mathcal{PT} -broken regimes. We also derive the real form of the G-function, which accounts for the real eigenvalues in the \mathcal{PT} -unbroken phase. Using this real G-function and its first-order derivative, we can analytically detect the EPs, at which both the G-function and its first-order derivative with respect to the eigenvalues are simultaneously zero. The previous AA method can be formulated within the current BOA scheme by considering the transitions between the same manifolds. Furthermore, we improve the AA method by additionally incorporating the transitions among the nearest-neighboring manifolds. Compared to the exact solutions, the present CAA improve the eigenvalues, more importantly, the eigenstates over the AA in both the \mathcal{PT} -symmetric and \mathcal{PT} -broken regimes.

We then study the VRS and atomic dynamics using the CAA in the PTQRM in various coupling regime and different imaginary biases. The emission spectrum shows two main peaks with unequal height in the ultrastrong coupling regime. The VRS becomes of multi-Rabi frequencies with increased coupling strength and higher biases. The width of the peaks also increase with the coupling strength and the imaginary biases, reflecting the nature of the open quantum systems, such as the atom-cavity coupling systems dissipating in the environment. This is due to the non-Hermitian description inheriting the nature of the Markov dynamics of the dissipative sys-

tems. Interestingly, the CAA results agree well with exact solution in all cases, indicating the CAA, where the transitions within the same manifold and between the nearest-neighboring manifolds are considered, captures the main features of the atomic dynamics and emission spectrum in this non-Hermitian light-matter interaction systems. In contrast, the AA completely fail to describe the dynamics of the this system, indicating the transition between the same manifold is insufficient to describe the dynamics. It is suggested that the present prediction for the VRS could be observed in the experiments that this model might be realized.

Finally, we also calculate the QFI of the PTQRM, which indicates that quantum criticality-enhanced effects also exist in this non-Hermitian system. Interestingly, near the EPs, the QFI in the PTQRM is much higher than that in its Hermitian counterpart. More interestingly, compared to the NH-TLS, the QFI is significantly enhanced in the PTQRM in the deep-strong coupling regime. The latter is just a NH-TLS coupled with a cavity, indicating that the atom-cavity coupling can enhance the sensitivity, providing a new way to increase the estimation precision.

In summary, we have proposed analytical methods to solve a class of many-body non-Hermitian quantum systems, bridging the gap between Hermitian and non-Hermitian systems, as well as between simple and complex non-Hermitian systems. We expect that the VRS could be also observed in this non-Hermitian atom-cavity coupling systems. We show that a simple non-Hermitian system, further coupled with a new degree of freedom,

provides a new avenue to increase quantum sensitivity, serving as a cornerstone for future exploration.

ACKNOWLEDGMENTS

This work is supported by the National Key R&D Program of China (Grant No. 2024YFA1408900) and the National Science Foundation of China (Grants No. 12305032).

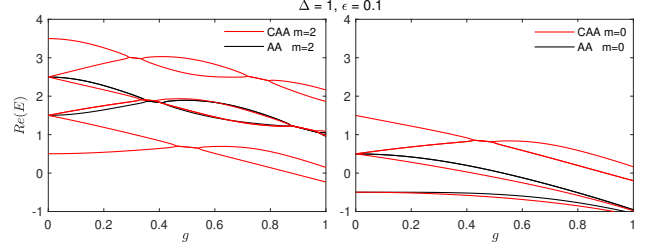


FIG. 9: (colored online) The real part of the eigenvalues given by CAA and AA as a function of coupling strength g at resonance ($\Delta = 1$), with $\epsilon = 0.1$. The left panel displays the results of $m = 2$, while the right panel shows results for $m = 0$. The black lines represent AA results, while the red lines denote CAA results.

APPENDIX: CAA METHOD

In the CAA, the m -th pair of eigenvalues can be obtained by select the following determinant in a 6-by-6 block form

$$\begin{vmatrix} \Omega_{m-1}^+(E) & 0 & 0 & -D_{m-1,m-1} & -D_{m-1,m} & -D_{m-1,m+1} \\ 0 & \Omega_m^+(E) & 0 & -D_{m-1,m} & -D_{m,m} & -D_{m,m+1} \\ 0 & 0 & \Omega_{m+1}^+(E) & -D_{m-1,m+1} & -D_{m,m+1} & -D_{m+1,m+1} \\ -D_{m-1,m-1} & -D_{m-1,m} & -D_{m-1,m+1} & \Omega_{m-1}^-(E) & 0 & 0 \\ -D_{m-1,m} & -D_{m,m} & -D_{m,m+1} & 0 & \Omega_m^-(E) & 0 \\ -D_{m-1,m+1} & -D_{m,m+1} & -D_{m+1,m+1} & 0 & 0 & \Omega_{m+1}^-(E) \end{vmatrix} = 0. \quad (28)$$

Note that for $m = 0$, the corresponding determinant takes a $4 - by - 4$ block form, because the $m = -1$ manifold does not exist. The determinant yields six roots for $m > 0$ and four roots for $m = 0$, but only two are required for any m . As we mentioned in the main text, the CAA eigenvalues should match the AA eigenvalues. As a detailed example, Figure 9 shows six (four) groups of the real roots for $m = 2(m = 0)$ in the left (right) panel.

Two solutions for real eigenvalues in the AA are also collected. One can immediately see that the third and the fourth roots (the first and the second roots) of the determinant fit the corresponding real eigenvalues levels of the AA for $m > 0(m = 0)$, while the other solutions are far from the AA results. This selection rule applies to arbitrary m . The corresponding imaginary parts of these two roots can also be calculated simultaneously.

[1] C. M. Bender and S. Boettcher, Phys. Rev. Lett. **80**, 5243 (1998).

[2] W. D. Heiss, Journal of Physics A: Mathematical and General **37**, 2455 (2004).

- [3] A. Mostafazadeh and A. Batal, *Journal of Physics A: Mathematical and General* **37**, 11645 (2004).
- [4] C. M. Bender, *Reports on Progress in Physics* **70**, 947 (2007).
- [5] Y. Ashida, Z. Gong, and M. Ueda, *Advances in Physics* **69**, 249 (2020).
- [6] C. M. Bender and D. W. Hook, (2023), arXiv:2312.17386 [quant-ph].
- [7] R. El-Ganainy, K. G. Makris, M. Khajavikhan, Z. H. Musslimani, S. Rotter, and D. N. Christodoulides, *Nature Physics* **14**, 11 (2018).
- [8] V. Meden, L. Grunwald, and D. M. Kennes, *Reports on Progress in Physics* **86**, 124501 (2023).
- [9] Y. N. Joglekar, R. Marathe, P. Durganandini, and R. K. Pathak, *Physical Review A* **90**, 040101 (2014).
- [10] T. E. Lee and Y. N. Joglekar, *Physical Review A* **92**, 042103 (2015).
- [11] Q. Xie, S. Rong, and X. Liu, *Physical Review A* **98**, 052122 (2018).
- [12] Y. Liu, L. Duan, and Q.-H. Chen, (2024), arXiv:2412.02918 [quant-ph].
- [13] T. Frith, *Journal of Physics A: Mathematical and Theoretical* **53**, 485303 (2020).
- [14] Z. Tian, Z.-X. Man, and B. Zhu, *Journal of Physics B: Atomic, Molecular and Optical Physics* **56**, 095001 (2023).
- [15] X. Ou, J. Huang, and C. Lee, *Chinese Physics B* **30**, 110309 (2021).
- [16] J. Li, Y.-C. Wang, L.-W. Duan, and Q.-H. Chen, (2024), arXiv:2402.09749.
- [17] X. Lu, H. Li, J.-K. Shi, L.-B. Fan, V. Mangazeev, Z.-M. Li, and M. T. Batchelor, *Physical Review A* **108**, 053712 (2023).
- [18] M. Naghiloo, M. Abbasi, Y. N. Joglekar, and K. Murch, *Nature Physics* **15**, 1232 (2019).
- [19] F. Yoshihara, T. Fuse, S. Ashhab, K. Kakuyanagi, S. Saito, and K. Semba, *Nature Physics* **13**, 44 (2017).
- [20] W.-C. Wang, Y.-L. Zhou, H.-L. Zhang, J. Zhang, M.-C. Zhang, Y. Xie, C.-W. Wu, T. Chen, B.-Q. Ou, W. Wu, H. Jing, and P.-X. Chen, *Phys. Rev. A* **103**, L020201 (2021).
- [21] J. Kim, T. Ha, D. Kim, D. Lee, K.-S. Lee, J. Won, Y. Moon, and M. Lee, *Applied Physics Letters* **123**, 161104 (2023).
- [22] M.-L. Cai, Z.-D. Liu, W.-D. Zhao, Y.-K. Wu, Q.-X. Mei, Y. Jiang, L. He, X. Zhang, Z.-C. Zhou, and L.-M. Duan, *Nature communications* **12**, 1126 (2021).
- [23] Q.-H. Chen, C. Wang, S. He, T. Liu, and K.-L. Wang, *Physical Review A* **86**, 023822 (2012).
- [24] L. Duan, Y.-F. Xie, and Q.-H. Chen, *Scientific Reports* **9**, 18353 (2019).
- [25] Y.-F. Xie and Q.-H. Chen, *Physical Review Research* **3**, 033057 (2021).
- [26] J. J. Sanchez-Mondragon, N. B. Narozhny, and J. H. Eberly, *Physical Review Letters* **51**, 550 (1983).
- [27] V. Giovannetti, S. Lloyd, and L. Maccone, *Nature Photonics* **5**, 222 (2011).
- [28] R. Di Candia, F. Minganti, K. V. Petrovnin, G. S. Paraoanu, and S. Felicetti, *npj Quantum Information* **9**, 23 (2023).
- [29] X. Yu and C. Zhang, *Physical Review A* **108**, 022215 (2023).
- [30] Z.-J. Ying, W.-L. Wang, and B.-J. Li, *Physical Review A* **110**, 033715 (2024).
- [31] Z.-P. Liu, J. Zhang, K. zdemir, B. Peng, H. Jing, X.-Y. L, C.-W. Li, L. Yang, F. Nori, and Y.-x. Liu, *Physical Review Letters* **117**, 110802 (2016).
- [32] S. Yu, Y. Meng, J.-S. Tang, X.-Y. Xu, Y.-T. Wang, P. Yin, Z.-J. Ke, W. Liu, Z.-P. Li, Y.-Z. Yang, G. Chen, Y.-J. Han, C.-F. Li, and G.-C. Guo, *Physical Review Letters* **125**, 240506 (2020).
- [33] Q. Liao, C. Leblanc, J. Ren, F. Li, Y. Li, D. Solnyshkov, G. Malpuech, J. Yao, and H. Fu, *Physical Review Letters* **127**, 107402 (2021).
- [34] W. Ding, X. Wang, and S. Chen, *Physical Review Letters* **131**, 160801 (2023).
- [35] Y.-Y. Wang, C.-W. Wu, W. Wu, and P.-X. Chen, *Physical Review A* **109**, 062611 (2024).
- [36] D. Braak, *Phys. Rev. Lett.* **107**, 100401 (2011).
- [37] Y.-Y. Zhang, Q.-H. Chen, and Y. Zhao, *Physical Review A* **87**, 033827 (2013).
- [38] Z.-M. Li and M. T. Batchelor, *Journal of Physics A: Mathematical and Theoretical* **48**, 454005 (2015).
- [39] S. Ashhab, *Physical Review A* **101**, 023808 (2020).
- [40] V. V. Mangazeev, M. T. Batchelor, and V. V. Bazhanov, *Journal of Physics A: Mathematical and Theoretical* **54**, 12LT01 (2021).
- [41] Z.-M. Li and M. T. Batchelor, *Physical Review A* **103**, 023719 (2021).
- [42] Y.-F. Xie and Q.-H. Chen, *Journal of Physics A: Mathematical and Theoretical* **55**, 225306 (2022).
- [43] D. Braak, *Symmetry* **11**, 1259 (2019).
- [44] R. J. Glauber, *Phys. Rev.* **131**, 2766 (1963).
- [45] Z.-M. Li and M. T. Batchelor, *Physical Review A* **104**, 033712 (2021).
- [46] J. B. Fraleigh, *A first course in abstract algebra* (Pearson Education India, 2003).
- [47] G. S. Agarwal, *Physical Review Letters* **53**, 1732 (1984).
- [48] R. J. Thompson, G. Rempe, and H. J. Kimble, *Physical Review Letters* **68**, 1132 (1992).
- [49] A. Boca, R. Miller, K. M. Birnbaum, A. D. Boozer, J. McKeever, and H. J. Kimble, *Physical Review Letters* **93**, 233603 (2004).
- [50] D. C. Brody, *Journal of Physics A: Mathematical and Theoretical* **47**, 035305 (2014).
- [51] Y.-Y. Zhang, Q.-H. Chen, and S.-Y. Zhu, *Chinese Physics Letters* **30**, 114203 (2013).
- [52] J. George, T. Chervy, A. Shalabney, E. Devaux, H. Hiura, C. Genet, and T. W. Ebbesen, *Physical Review Letters* **117**, 153601 (2016).
- [53] M. Orszag, *Quantum Optics: Including Noise Reduction, Trapped Ions, Quantum Trajectories, and Decoherence* (Springer International Publishing, Cham, 2024).
- [54] F. Roccati, G. M. Palma, F. Ciccarello, and F. Bagarello, *Open Systems & Information Dynamics* **29**, 2250004 (2022).
- [55] S. L. Braunstein and C. M. Caves, *Phys. Rev. Lett.* **72**, 3439 (1994).
- [56] J. S. Sidhu and P. Kok, *AVS Quantum Science* **2**, 014701 (2020).
- [57] J.-F. Ren, J. Li, H.-T. Ding, and D.-W. Zhang, *Physical Review A* **110**, 052203 (2024).